RESEARCH LETTER

Association of Space Flight With Problems of the Brain and Eyes

Space flight-associated neuroocular syndrome (SANS), characterized by increased optic nerve sheath diameter (ONSD) and globe flattening, is detected in some astronauts.[1] Because inflight cerebrospinal fluid (CSF) pressure measurement is excessively invasive, it is not realistic to conduct. We estimated CSF pressure (p_{CSF}) during space flight based on published reports[2] and found that SANS was not caused mainly by increased p_{CSF} but rather by brain upward shift (BUS), recently demonstrated in postflight astronauts.[3] Our findings suggest that eyes are portals into effects on the brain during space flight.

Methods | We created a model of the optic nerve sheath (ONS) as a tube including a cylinder (**Figure 1**). This modeling allowed us to apply the material mechanics theory of thin-walled tubes. This study used published data and institutional review board approval was not required. The r_{ONS} rise due to increased p_{CSF} ($p_O+\Delta p$) is expressed as: $\Delta r_{ONS}(\Delta p) = r_{ONS}(p_O+\Delta p) - r_{ONS}(p_O)$, in which p_O and $r_{ONS}(p_O)$ are taken as standard values of p_{CSF} and r_{ONS}, respectively. Thus, ONS deformation (ε) is defined as: $\varepsilon(\Delta p) = \Delta r_{ONS}(\Delta p) / r_{ONS}(p_O)$. This procedure enables us to estimate p_{CSF} from r_{ONS}, which is measurable by ultrasonography[1] during space flight. To derive parameters that represent the mechanical strength of ONS tissues, the anatomical data of Hansen et al[2] were used. We also used the inflight ONSD[1] value of 12 mm and the human standard ONSD value[1] of 5.9 mm for these calculations.

Results | The ε in our ONS model was 0.15 by a pressurization (Δp) of 5 mm Hg, and increased proportionally with further pressurization. Assuming a linear relation between ε and Δp according to the material mechanics, the formula $\varepsilon(\Delta p) = 4.0 \times 10^{-3}\Delta p + 0.16$ was obtained by linear fitting with the data of Hansen et al[2] for $\Delta p > 10$ mm Hg. Hence we obtained $\Delta p = 210$ mm Hg from the calculation of $\varepsilon = (12-5.9) / 5.9 \cong 1.0$ for an inflight astronaut.[1] This p_{CSF} value, which exceeds the human standard value, suggests a substantial deterioration of the elasticity of the ONS, and the origin of this deterioration is discussed in the following section.

Discussion | Because postflight sagittal magnetic resonance images of astronauts show an uplifting of the optic chiasm,[3] it is assumed that the optic nerve (ON) is pulled rearward according to the BUS along with brain rotation around the edge of the cerebellar tentorium during space flight (**Figure 2**A). This rearward shift of the ON may result in an expansion and bending of the ONS (ie, increased ONSD) because the periosteum is connected to the dura of the ONS at the orbit (Figure 2B). Furthermore, this rearward force on the ON yields a deformation of the eyeball (ie, globe flattening) because of the restoration force of the dura on the eyeball (Figure 2C). This is because the dura of the ONS is known to be as hard as the ocular sclera. Our hypotheses are consistent with the globe flattening that typically affects both eyes[1] and the downward deflection of the Bruch membrane opening.[4]

Barratt[5] reported that his standing height during space flight reverted to a preflight baseline within 3 hours in response to him wearing a penguin suit or in combination with heavy resistive exercise. This height reversion is attributed to the recovery of the thoracic curve[5] that is induced by these compressions. This may raise p_{CSF} because of the associated reduction of total subarachnoid volume. The redundant CSF accumulates in the extracranial portion of the ONS, where the volume is more easily changed than in the intracranial portion. Therefore, one might reconsider wearing a penguin suit repeatedly and performing resistive exercise during space-flight.

Conclusions | Our model enables us to estimate p_{CSF} from ONSD. However, the estimated p_{CSF} suggests that the model is invalid for some astronauts because their ONS tissues may be changed by BUS. Furthermore, compression forces that reduce subarachnoid volume exacerbate SANS.

Figure 1. Cross-sectional View of the Modeled Optic Nerve Sheath

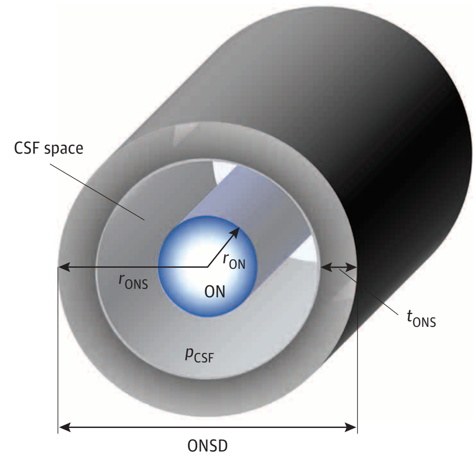

We define optic nerve sheath radius (r_{ONS}) as r_{ONS} = optic nerve sheath diameter (ONSD) / 2 as a function of cerebrospinal fluid pressure (p_{CSF}). We assume that r_{ONS} depends on p_{CSF}, while optic nerve radius (r_{ON}) and dura thickness (t_{ONS}) do not. The introduction of the deformation (ε) facilitates the estimation of p_{CSF} because ε is a ratio of an increased ONSD to a standard ONSD. CSF indicates cerebrospinal fluid.

Figure 2. Theoretical Inflight and Postflight Conditions of Optic Nerve

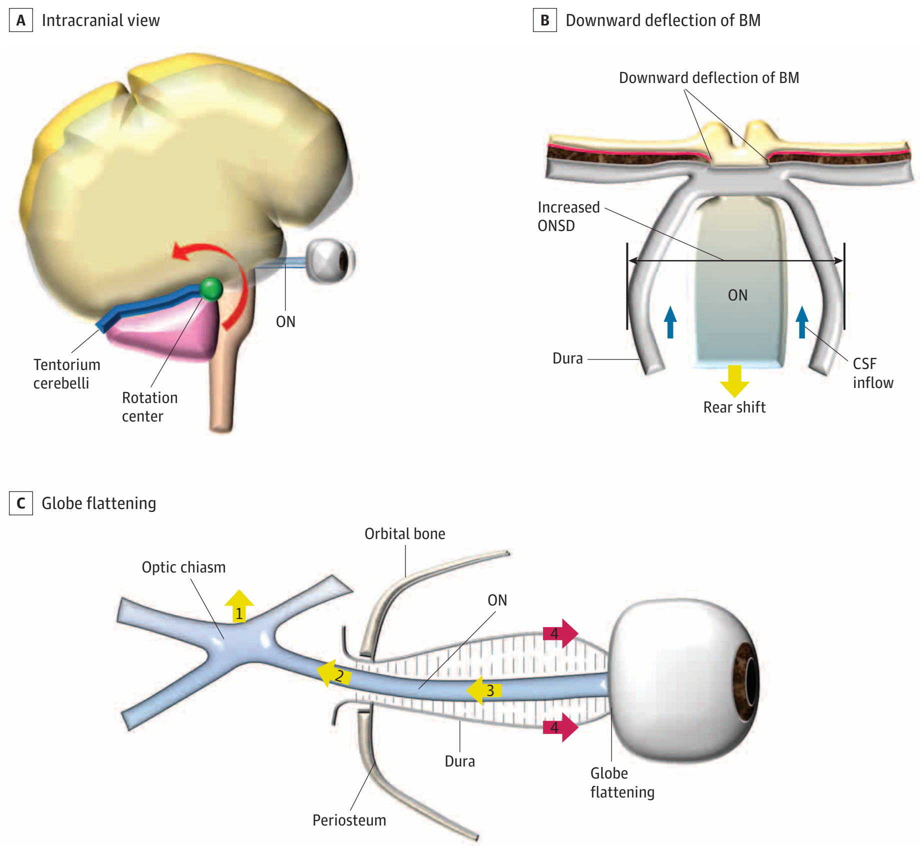

A, Intracranial views from the right side. The cerebellum is caught in part of the tentorium cerebelli because of brain upward shift during space flight, and the cerebrum thereby rotates counter-clockwise with a narrowing of the cerebrospinal fluid (CSF) spaces at the vertex. The gray shading indicates the original position in the 1*g* terrestrial environment. B and C, The hypothesis for the increased optic nerve sheath diameter (ONSD) and the globe flattening is illustrated. The optic nerve (ON) shifts rearward as the brain shifts upward, resulting in globe flattening and the deformation of the dura. In addition, the Bruch membrane (BM) is deflected downward. The yellow arrowheads indicate the (1) uplifting of the optic chiasm accompanied by brain upward shift, that (2) the portion of the ON from the optic chiasma to the optic canal is pulled rearward and upward, and that (3) the other portion of the ON from the optic canal to the eyeball shifts rearward, while the red arrowheads indicate that (4) the restoration force of the dura on the eyeball results in globe flattening (C).

Ari Shinojima, MD, PhD
Itsuhiro Kakeya, PhD
Satoru Tada, MD, PhD

Author Affiliations: Department of Ophthalmology, Lariboisière Hospital, Assistance Publique-Hôpitaux de Paris, University Sorbonne Paris Cité, Paris, France (Shinojima); Department of Electronic Science and Engineering, Kyoto University, Kyotodaigaku-Katsura, Nishikyo, Kyoto, Japan (Kakeya); Department of Neurology, Osaka University Graduate School of Medicine, 2-2 Yamadaoka, Suita, Japan (Tada).

Corresponding Author: Ari Shinojima, MD, PhD, Department of Ophthalmology, Lariboisière Hospital, Assistance Publique-Hôpitaux de Paris, University Sorbonne Paris Cité, 2 Rue Ambroise Paré, Paris 75010, France (shinojima.ari@nihon-u.ac.jp).

Published Online: July 5, 2018. doi:10.1001/jamaophthalmol.2018.2635

Author Contributions: Dr Shinojima had full access to all of the data in the study and takes responsibility for the integrity of the data and the accuracy of the data analysis. All authors contributed equally to this report.
Concept and design: Shinojima, Kakeya.
Acquisition, analysis, or interpretation of data: All authors.
Drafting of the manuscript: All authors.
Critical revision of the manuscript for important intellectual content: Shinojima, Kakeya.
Supervision: Kakeya, Tada.

Conflict of Interest Disclosures: All authors have completed and submitted the ICMJE Form for Disclosure of Potential Conflicts of Interest and none were reported.

Additional Contributions: We thanks Ramin Tadayoni, MD, PhD, Lariboisière Hospital, for allowing this article to be written. He was not compensated for his contribution.

1. Brunstetter T. Introduction to space flight-associated neuro-ocular syndrome (SANS). https://ntrs.nasa.gov/archive/nasa/casi.ntrs.nasa.gov/20170009173.pdf. Accessed February 28, 2018.

2. Hansen HC, Lagrèze W, Krueger O, Helmke K. Dependence of the optic nerve sheath diameter on acutely applied subarachnoidal pressure—an experimental ultrasound study. *Acta Ophthalmol*. 2011;89(6):e528-e532. doi:10.1111/j.1755-3768.2011.02159.x

3. Roberts DR, Albrecht MH, Collins HR, et al. Effects of spaceflight on astronaut brain structure as indicated on MRI. *N Engl J Med*. 2017;377(18):1746-1753. doi:10.1056/NEJMoa1705129

4. Patel N, Pass A, Mason S, Gibson CR, Otto C. Optical coherence tomography analysis of the optic nerve head and surrounding structures in long-duration International Space Station astronauts. [published online January 11, 2018]. *JAMA Ophthalmol*. 2018;136(2):193-200. doi:10.1001/jamaophthalmol.2017.6226

5. Barratt MR. 63rd Louis H. Bauer Lecture. Aerospace Medical Association: the 88th Annual Scientific Meeting. https://www.asma.org/asma/media/AsMA/home-page-rotator/Annual%20Meeting/63rd-Bauer-Lecture.mp4. Accessed February 28, 2018.

OBSERVATION

Choroideremia in a Woman With Turner Syndrome

Report of a Case | A 67-year-old woman with a previous clinical diagnosis of retinal degeneration and a family history of choroideremia (CHM) (**Figure 1**) was referred to the Moran Eye Center for further evaluation. The patient reported experiencing gradual peripheral vision loss and nyctalopia over many years and was recently declared legally blind.

Applied Physics Letters

Circularly polarized terahertz radiation monolithically generated by cylindrical mesas of intrinsic Josephson junctions

Cite as: Appl. Phys. Lett. **113**, 052601 (2018); https://doi.org/10.1063/1.5040159
Submitted: 15 May 2018 . Accepted: 17 July 2018 . Published Online: 30 July 2018

Asem Elarabi, Yusuke Yoshioka, Manabu Tsujimoto, and Itsuhiro Kakeya

Circularly polarized terahertz radiation monolithically generated by cylindrical mesas of intrinsic Josephson junctions

Asem Elarabi,[1,a)] Yusuke Yoshioka,[1] Manabu Tsujimoto,[1,2] and Itsuhiro Kakeya[1,a)]
[1]Department of Electronic Science and Engineering, Kyoto University, Nishikyo, Kyoto 615-8510, Japan
[2]Faculty of Pure and Applied Sciences, University of Tsukuba, 1-1-1 Tennodai, Tsukuba, Ibaraki 305-8573, Japan

(Received 15 May 2018; accepted 17 July 2018; published online 30 July 2018)

We report emissions of circular polarized electromagnetic waves from cylindrically shaped mesa structures of the high-temperature superconductor $Bi_2Sr_2CaCu_2O_{8+\delta}$. The frequency range of circularly polarized emission of a cylindrical mesa with notched sides is between 400 and 430 GHz, which is wider than expected by the patch antenna theory. Three maxima recognized in emission intensity are presumably attributed to excitations of fundamental orthogonal modes and circularly polarized modes. Along with the demonstration of circularly polarized emission from truncated edge square mesas, the obtained results provide a wide variety of engineering designs of compact and solid-state electromagnetic sources which are able to generate circularly-polarized terahertz waves. *Published by AIP Publishing.* https://doi.org/10.1063/1.5040159

The terahertz (THz) frequency range of 0.3–3 THz is considered as the last understudied range in the electromagnetic (EM) spectrum owing to the lack of efficient and powerful sources. Numerous applications are made possible as a result of the active research in the field.[1,2] Many of these applications exploit the penetration and absorption of materials to the terahertz radiation for imaging in medical, industrial, scientific, and defense purposes. Other applications may employ the radiation to identify materials as the THz frequency range matches many absorption lines for various chemicals. Furthermore, other applications are made possible such as high-resolution radars for remote sensing, space telecommunication, and for scientific experiments to study non-equilibrium dynamics of complex matter.[2,3] After the discovery of a new class of terahertz emitters based on the high-T_c superconductor $Bi_2Sr_2CaCu_2O_{8+\delta}$ (Bi2212) in 2007,[4] a large number of studies were conducted to increase its power,[5–7] broaden its frequency tunability,[8–12] and increase the operation temperature.[13] One of the remaining challenging topics in the terahertz sources, especially for Bi2212-based sources, is the control of the polarization of the generated EM waves.[14] Monolithic control of the polarization has a great significance in fields of mobile communications to reduce the polarization loss, circular dichroism spectroscopy, and polarized imaging for cancer detection.[15] Furthermore, recent studies have shown that circular polarization (CP) can be achieved in several terahertz sources through the surface manipulation of the generated emission;[16–18] however, simpler, and more effective methods were proposed numerically[19–21] and achieved experimentally[22] by using Bi2212-based devices.

The application of a voltage across the *c*-axis of a Bi2212 mesa structure composed of stacked intrinsic Josephson junctions (IJJs) causes the IJJs to oscillate according to the ac Josephson relation, $f_j = 2eV/(Nh)$, where V is the dc voltage applied across N IJJs, e is the elementary charge, and h is Planck's constant. The use of a mesa with a thickness of $t \approx 1\mu$m results in the oscillation frequency in the terahertz range. The synchronization of a thousand IJJs, in addition to the cavity resonance of the mesa geometry, plays the main role in generating high-intensity radiation observed in such sources.

Terahertz emission from cylindrical mesas has gained interest[23–26] owing to a special property of thin cylindrical mesas. The standing EM mode frequency values f^c_{mp} [m represents the number of nodes along the diameter and p accounts for the number of zeros of the first derivative of the regular Bessel function $J_1(z)$[27]] of such mesas are incommensurate with the harmonic ac Josephson frequencies nf_j, where n is an integer.[23,24] Therefore, the frequency values of the cylindrical cavity mode and ac Josephson frequency can only be matched at a single frequency. Terahertz radiation mechanisms were studied theoretically and experimentally by measuring the radiation patterns of cylindrical and rectangular mesas.[23,24,28] A dual-source mechanism of a uniform ac Josephson oscillation and a nonuniform single EM cavity resonance mode was proposed with the uniform source as the primary source of radiation.[24,29] Furthermore, the variation in the mesa geometrical shape,[30] dimensions,[31] and bias feeding point[7] was recently studied. Recently, a cylindrical mesa device with a wide tuning range of 0.5–2.4 THz was achieved.[8] The large tunability range is considered to be due to proximities of values in f^c_{mp}.

In this study, we experimentally present direct evidence that a single EM cavity mode in cylindrical mesas is a highly effective source of radiation, enough to control the polarization of the emitted waves. We designed cylindrical mesas with small notched sides to control the polarization. A circularly polarized radiation with a low axial ratio (AR) is experimentally demonstrated from the cylindrical mesa geometry. In addition, the evolution of emission spectra in the CP region was revealed.

Figures 1(a)–1(c) show schematic drawings and an optical image for mesa geometry used in the study. The mesa was shaped by using photolithography and Ar ion-beam

a)Authors to whom correspondence should be addressed: asemelarabi@sk.kuee.kyoto-u.ac.jp and kakeya@kuee.kyoto-u.ac.jp

milling techniques on a thin, cleaved Bi2212 single crystal covered with a thin silver layer of ~30 nm. The Bi2212 single crystal was glued using a stycast to a sapphire substrate. A thin layer of CaF_2 was used as an insulating barrier between the silver electrodes and the mesa side-wall to prevent current leakage. Current flows from the silver electrodes at the top of the mesa through its *c*-axis to the ground electrodes on the surface of the base crystal. The mesa-shaped design is based on the circular-notched microstrip patch antenna.[32,33] The CP in this design was realized by tuning the perturbation area ΔS to excite two degenerate orthogonal transverse modes TM_{11a} and TM_{11b} along the major and minor diagonals, respectively [Modes 1 and 2 in Fig. 1(a)].[33] As these two modes have slightly different resonance frequencies, the mesa shape was designed with a perturbation to allow the two modes to merge at the collective cavity resonance frequency with a 90° phase difference, thus forming a rotating surface current. The frequencies of the two mentioned modes were determined as follows:[33] $f_{11a} = f_{11}\left(1 + 0.4185\frac{\Delta S}{S}\right), f_{11b} = f_{11}\left(1 - 1.4185\frac{\Delta S}{S}\right)$, where S is the total area of the disk before notching. The standing EM mode frequency f_{11} of the mesa was determined by $f_{11} = \chi_{11}c_0/\left(2\pi\sqrt{\epsilon}a\right)$, where a is the disk radius, c_0 is the speed of light in vacuum, ϵ is the dielectric constant of Bi2212, and $\chi_{11} = 1.841$ is the lowest zero of the first derivative of the first-order Bessel function $J_1(z)$.[23,24] Emission of the terahertz wave was detected using a silicon bolometer, and its polarization was characterized by the detected intensity through a rotating wire grid polarizer (WGP) in the beam path. Emission spectra were obtained using a Fourier-transform interferometer with a pair of lamellar mirrors.[34]

In this study, two mesas with similar geometrical shapes and slightly different dimensions were used. Mesa 1 (2) has a radius of $a = 42$ (46) μm, a notched rectangular area with length $r_1 = 6.0$ (11.2) μm, a width $w = 16$ (20) μm, area ratio $\Delta S/S = 3.46 \times 10^{-2}$ (3.37×10^{-2}), and a mesa thickness $t = 1.9$ (2.3) μm. The feeding electrodes were placed on the sides of the mesa at a 45° angle of the major diagonal. Based on these geometries and a fitting value of $\epsilon = 21$, f_{11a}, f_{11b}, and f_{11} of mesa 1 (2) were estimated as 463 (422), 434 (396), and 456 (417) GHz, respectively.[35] Figure 2 presents the *I–V* curve and the detected emission of mesa 2, with $T_c = 85$ K. The *I–V* curve shows a typical behavior of slightly underdoped superconducting Bi2212 mesas. Strong emissions were detected from both samples with the highest emission power detected at the bolometer's window $P_{max} \approx 15.3$ and 70 nW for mesas 1 and 2, respectively. Broad emission ranges with three distinctive peaks implying TM_{11a}, TM_{11b}, and TM_{mean} [marked using different colors in Fig. (2)], were observed in both samples. Several discontinuities in the *I-V* curves attributed to partial retrappings, at which some of the IJJs revert to the zero-resistance state, were found in the emission region. This yields some ambiguity in the estimation of emission frequency from the bias voltage.

Polarization characteristics of the emissions were measured at the outermost branch of both *I–V* curves. The evolution of the polarization of mesas 1 and 2 is plotted in Figs. 3(a) and 3(c), which shows the axial ratio (AR), that is, the ratio between the major and minor axes of the fitted polarization ellipse, as a function of the bias voltage and frequency, respectively. An AR of less than 3 dB is generally regarded as circularly polarized.[36] The polarization evolution shows

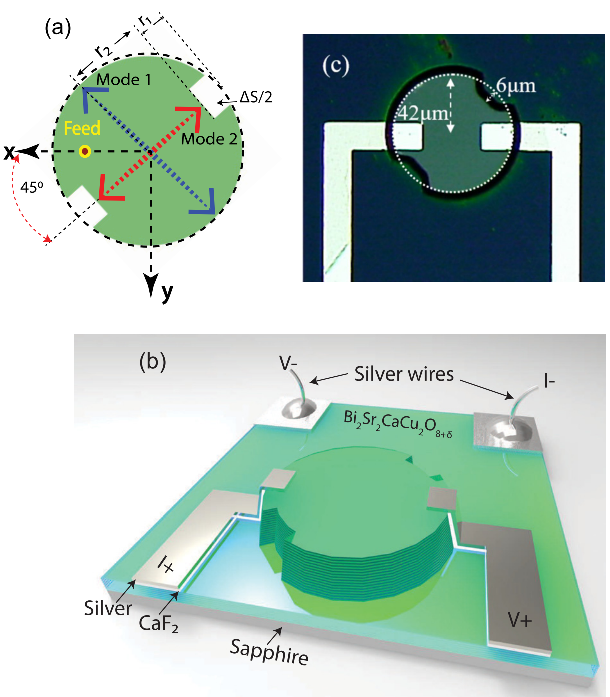

FIG. 1. (a) Plan drawing of an IJJ mesa for generation of circularly-polarized terahertz waves. The blue and red arrows indicate TM_{11a} and TM_{11b} mode standing waves, respectively. (b) Three-dimensional sketch of the sample including the electrodes, base crystal, and wiring. (c) Optical image of mesa 1.

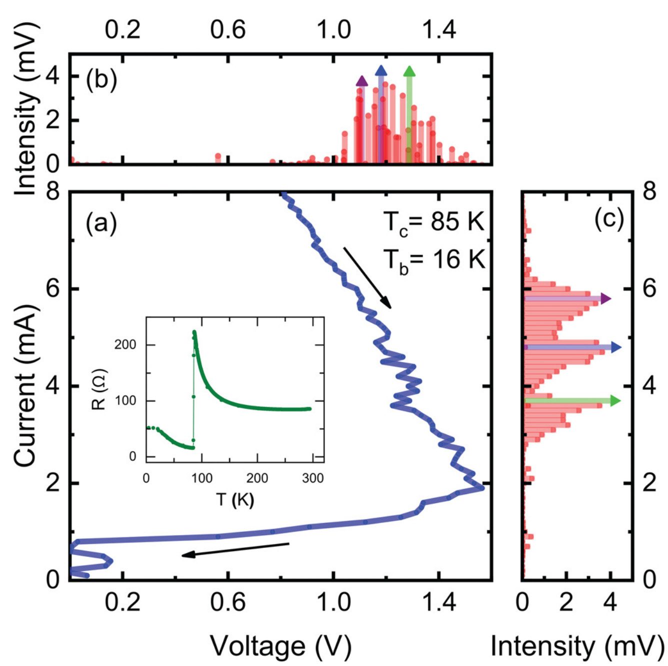

FIG. 2. Current-voltage characteristic (a) and detector responses as a function voltage (b) and current (c) of mesa 2 at $T_b = 16$ K. The inset of (a) shows the temperature dependence of resistance. Constant-current bias was used for measurements. The arrows in (a) represent the direction of bias scan. The colored arrows in (b) and (c) indicate the peaks in detection intensity implying excitations of TM_{11a}, TM_{11b}, and TM_{mean}.

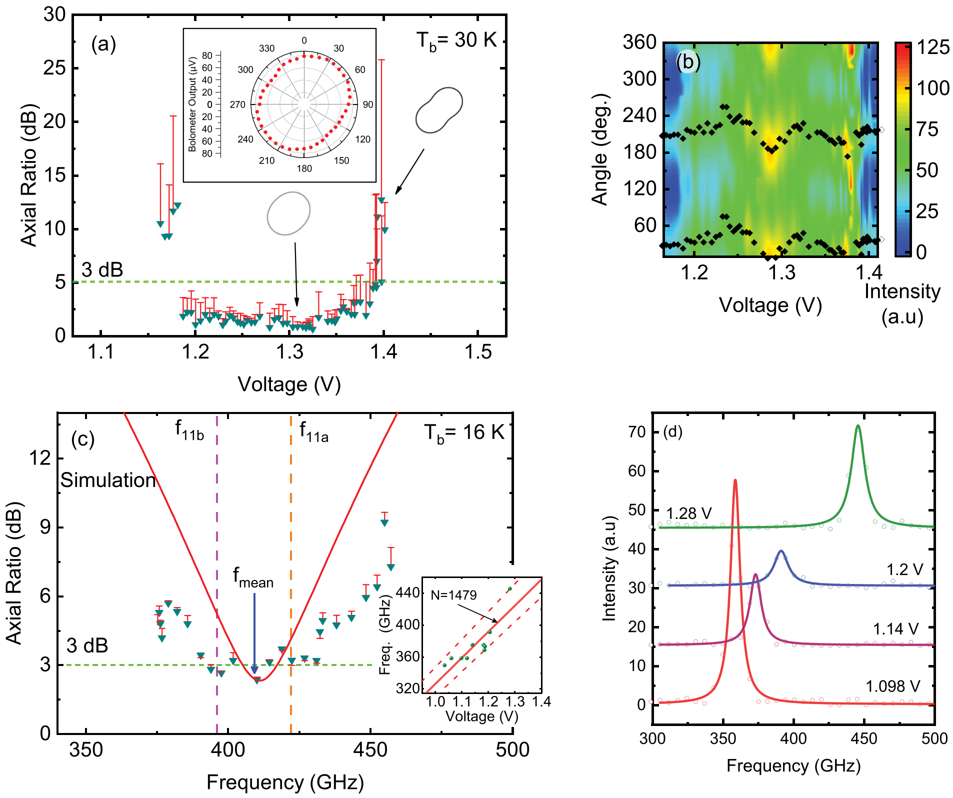

FIG. 3. (a) Voltage evolution of AR for mesa 1 at 30 K. The inset shows the detected intensity with respect to the WGP angle as a polar graph at a voltage which gives the minimum AR. The error bars are determined by the difference in the detected intensity ratio and fitting. (b) Measured voltage- and angular-dependent intensities for the entire emission range of mesa 1. The major axis angles are represented by black diamonds. (c) Frequency evolution of AR for mesa 2 at 16 K. A solid curve is a result of simulation with $\epsilon = 21$. The magenta and orange vertical dashed lines indicate the values of f_{11b}, and f_{11a}, respectively, while f_{11} is indicated by a blue vertical arrow. The inset shows frequency evolution in terms of bias voltage, the two dashed lines indicate the maximum and minimum estimated numbers of working junctions $N_{max} = 1553$ and $N_{min} = 1390$, the solid red line shows the best fitting with N = 1479. (d) Radiation spectra at $T_b = 16$ K at four different bias conditions.

an inverse bell-shaped characteristic commonly found in CP patch antennas with some oscillations caused by the retrapping of a part of IJJs reverting into the superconducting state. At $V_b = 1.31$ V, the minimum ARs for mesas 1 and 2 are $AR_{min} = 0.8$ and 2.37 dB, respectively. The inset of Fig. 3(a) depicts a polar plot showing the angle-dependent intensity (obtained through WGP) for mesa 1 at $V_b = 1.31$ V. Both samples had a comparable major axis angle of $\theta \approx 30°–40°$ at the AR_{min}.

The false-color 2D contour plot in Fig. 3(b) shows the observed voltage-dependent intensity distribution with respect to WGP angle θ for mesa 1. As depicted in the figure, the intensity was the highest at the range of the lowest AR values ($V_b = 1.39–1.18$ V). The major axis angle varies at different bias points. Furthermore, in the relatively higher AR range (over 1.5 dB), the angle tended to be in the range of 29°–35°, which is approximately along Mode 2 determined by the minor (notched) diameter. This trend was commonly found in mesa 2.

In mesa 2, the emission spectra were obtained at four different bias currents, as shown in Fig. 3(d). As depicted in red, the first frequency $f_1 = 360$ GHz was measured at the top intensity peak shown in the detected emission graph [Fig. 2(b)]; this corresponds to $I_b \approx 5.8$ mA. The frequency was measured at three other points covering the second and third peaks shown in Fig. 2(b). That is, $f_2 = 370$ GHz at $I_b = 5.2$ mA (purple), $f_3 = 390$ GHz at $I_b = 4.7$ mA (blue), and $f_4 = 445$ GHz at $I_b = 3.7$ mA (green). A noticeable degradation was observed in the emission intensity at the middle frequencies f_2 and f_3. This intensity degradation and broadening of the linewidth of the f_3 spectrum might correspond to the resonant modes inside the mesa geometry. Here, frequencies f_1 and f_4 might be closely approximated to the theoretical resonance frequencies f_{11b} and f_{11a}, respectively. Similarly, f_2 and f_3 should be closely related to frequency $f_{mean} = (f_{11a} + f_{11b})/2 = 409$ GHz, which is the frequency of the collective mode at which the CP is manifested.

To discuss frequency evolution of polarization, emission frequencies were estimated precisely considering the change in the number of IJJs contributing to the emission according to the ac Josephson relation. The inset of Fig. 3(c) shows the emission frequency in terms of the measured voltage. The two red-dashed lines represent the frequency according to the Josephson relation when the number of working junctions $N_{max} = 1553$ and $N_{min} = 1390$. The red-solid line shows a fitting with $N = 1480$. This graph confirms that at some radiation ranges, most junctions contributed to the emission, while at other ranges, only a part of the junctions contributed.

For mesa 2, $f_1 = 0.91 f_{11b}$, $f_4 = 1.01 f_{11a}$, $f_2 = 0.9 f_{mean}$, and $f_3 = 0.95 f_{mean}$. The deviation of f_1 from f_{11a} is attributed to the trapezoidal cross-section of the mesa. As the bottom width of the mesa is approximately 15% longer than the top width, f_1 is closer to f_{11a} for the bottom geometry. In contrast, f_4 agrees with f_{11b} for the top geometry. Thus, the range of the emission frequency lies between the geometrical minimum and maximum frequencies. This supports our argument that the broad minimum in AR is attributed to the entrainment of resonance frequencies of the stacked IJJs. It can be expressed that the system selects an emission frequency so as to have minimum AR.

For mesa 1, emission frequencies can be estimated from V_b and the thickness of the mesa. As a result, CP, where AR is less than 3 dB, is demonstrated in a frequency range of

450–520 GHz. The difference in the AR_{min} is attributed to the difference in the volume of mesas. For mesas 1 and 2, the values of $\Delta S/S$ are almost the same, that is, 3.46% and 3.37%, while their AR_{min} values are considerably different, that is, 0.8 and 2.3, respectively. The requirement to have a perfect CP with AR = 0 dB for a notched circular antenna is $\Delta S/S = (Q_0\chi_{11})^{-1}$, where Q_0 is the unloaded quality factor of the antenna. As Q_0 can be regarded as a cavity quality factor of a mesa, an approximate difference of 20% in mesa thickness can be considered as a dominant factor to explain the difference in AR_{min}.

In conclusion, the generation of circularly polarized terahertz waves was demonstrated using cylindrical mesas with notched sides in addition to truncated-edge square mesas proposed in a previous work.[22] CP with AR <3 dB was attained in both samples, and emission spectra at various bias voltages from elliptical to CP were obtained. The series of emission spectra allowed the determination of the frequency evolution of AR, which is found to be roughly consistent with the patch antenna theory. We revealed the widening of the minimum AR range presumably due to entrainment of resonance frequencies of different geometrical parameters. The major axis tends to be along the notch direction, and the difference in the minimum AR is attributed to the difference in the volume of mesas. Applications of this type of terahertz sources may include quantum cryptography, spectroscopy, and imaging.

This work was supported by KAKENHI No. 5KK0204 and Murata Science Foundation. The authors would like to thank K. Kadowaki, T. Kashiwagi, F. Tubbal, H. Minami, R. Morita, S. Dhillon, and J. Tignon for the fruitful discussions. The Bi2212 single crystals are provided by Y. Nakagawa and Y. Nomura.

[1]M. Tonouchi, Nat. Photonics **1**, 97 (2007).
[2]S. S. Dhillon, M. S. Vitiello, E. H. Linfield, A. G. Davies, M. C. Hoffmann, J. Booske, C. Paoloni, M. Gensch, P. Weightman, G. P. Williams, E. Castro-Camus, D. R. S. Cumming, F. Simoens, I. Escorcia-Carranza, J. Grant, S. Lucyszyn, M. Kuwata-Gonokami, K. Konishi, M. Koch, C. A. Schmuttenmaer, T. L. Cocker, R. Huber, A. G. Markelz, Z. D. Taylor, V. P. Wallace, J. Axel Zeitler, J. Sibik, T. M. Korter, B. Ellison, S. Rea, P. Goldsmith, K. B. Cooper, R. Appleby, D. Pardo, P. G. Huggard, V. Krozer, H. Shams, M. Fice, C. Renaud, A. Seeds, A. Stöhr, M. Naftaly, N. Ridler, R. Clarke, J. E. Cunningham, and M. B. Johnston, J. Phys. D: Appl. Phys. **50**, 043001 (2017).
[3]D. N. Basov, R. D. Averitt, D. Van Der Marel, M. Dressel, and K. Haule, Rev. Mod. Phys. **83**, 471 (2011).
[4]L. Ozyuzer, A. E. Koshelev, C. Kurter, N. Gopalsami, Q. Li, M. Tachiki, K. Kadowaki, T. Yamamoto, H. Minami, H. Yamaguchi, T. Tachiki, K. E. Gray, W.-K. Kwok, and U. Welp, Science **318**, 1291 (2007).
[5]X. J. Zhou, J. Yuan, H. Wu, Z. S. Gao, M. Ji, D. Y. An, Y. Huang, F. Rudau, R. Wieland, B. Gross, N. Kinev, J. Li, A. Ishii, T. Hatano, V. P. Koshelets, D. Koelle, R. Kleiner, H. B. Wang, and P. H. Wu, Phys. Rev. Appl. **3**, 044012 (2015).
[6]T. M. Benseman, K. E. Gray, A. E. Koshelev, W.-K. Kwok, U. Welp, H. Minami, K. Kadowaki, and T. Yamamoto, Appl. Phys. Lett. **103**, 022602 (2013).
[7]C. Watanabe, H. Minami, T. Kitamura, K. Asanuma, K. Nakade, T. Yasui, Y. Saiwai, Y. Shibano, T. Yamamoto, T. Kashiwagi, R. A. Klemm, and K. Kadowaki, Appl. Phys. Lett. **106**, 042603 (2015).
[8]T. Kashiwagi, K. Sakamoto, H. Kubo, Y. Shibano, T. Enomoto, T. Kitamura, K. Asanuma, T. Yasui, C. Watanabe, K. Nakade, Y. Saiwai, T. Katsuragawa, M. Tsujimoto, R. Yoshizaki, T. Yamamoto, H. Minami, R. A. Klemm, and K. Kadowaki, Appl. Phys. Lett. **107**, 082601 (2015).
[9]T. M. Benseman, A. E. Koshelev, K. E. Gray, W.-K. Kwok, U. Welp, K. Kadowaki, M. Tachiki, and T. Yamamoto, Phys. Rev. B **84**, 064523 (2011).
[10]K. Delfanazari, H. Asai, M. Tsujimoto, T. Kashiwagi, T. Kitamura, T. Yamamoto, M. Sawamura, K. Ishida, C. Watanabe, S. Sekimoto, H. Minami, M. Tachiki, R. A. Klemm, T. Hattori, and K. Kadowaki, Opt. Express **21**, 2171 (2013).
[11]E. A. Borodianskyi and V. M. Krasnov, Nat. Commun. **8**, 1742 (2017).
[12]M. Tsujimoto, Y. Maeda, H. Kambara, A. Elarabi, Y. Yoshioka, Y. Nakagawa, Y. Wen, T. Doi, H. Saito, and I. Kakeya, Supercond. Sci. Technol. **28**, 105015 (2015).
[13]H. Minami, C. Watanabe, T. Kashiwagi, T. Yamamoto, K. Kadowaki, and R. A. Klemm, J. Phys. Condens. Matter **28**, 025701 (2016).
[14]I. Kakeya and H. Wang, Supercond. Sci. Technol. **29**, 073001 (2016).
[15]P. Doradla, K. Alavi, C. Joseph, and R. Giles, J. Biomed. Opt. **18**, 090504 (2013).
[16]M. Song, H. Yu, J. Luo, and Z. Zhang, Plasmonics **12**, 649 (2017).
[17]G. Liang, Y. Zeng, X. Hu, H. Yu, H. Liang, Y. Zhang, L. Li, A. G. Davies, E. H. Linfield, and Q. J. Wang, ACS Photonics **4**, 517 (2017).
[18]P. Rauter, J. Lin, P. Genevet, S. P. Khanna, M. Lachab, A. Giles Davies, E. H. Linfield, and F. Capasso, Proc. Natl. Acad. Sci. **111**, E5623 (2014).
[19]A. Elarabi, Y. Yoshioka, M. Tsujimoto, Y. Nakagawa, and I. Kakeya, Phys. Procedia **81**, 133 (2016).
[20]H. Asai and S. Kawabata, Appl. Phys. Lett. **110**, 132601 (2017).
[21]H. Asai and S. Kawabata, IEEE Trans. Appl. Supercond. **26**, 1800804 (2016).
[22]A. Elarabi, Y. Yoshioka, M. Tsujimoto, and I. Kakeya, Phys. Rev. Appl. **8**, 064034 (2017).
[23]R. A. Klemm, E. R. Laberge, D. R. Morley, T. Kashiwagi, M. Tsujimoto, and K. Kadowaki, J. Phys. Condens. Matter **23**, 025701 (2011).
[24]M. Tsujimoto, K. Yamaki, K. Deguchi, T. Yamamoto, T. Kashiwagi, H. Minami, M. Tachiki, K. Kadowaki, and R. A. Klemm, Phys. Rev. Lett. **105**, 037005 (2010).
[25]T. Kashiwagi, M. Tsujimoto, T. Yamamoto, H. Minami, K. Yamaki, K. Delfanazari, K. Deguchi, N. Orita, T. Koike, R. Nakayama, T. Kitamura, M. Sawamura, S. Hagino, K. Ishida, K. Ivanovic, H. Asai, M. Tachiki, R. A. Klemm, and K. Kadowaki, Jpn. J. Appl. Phys. **51**, 010113 (2012).
[26]S. Guénon, M. Grünzweig, B. Gross, J. Yuan, Z. G. Jiang, Y. Y. Zhong, M. Y. Li, A. Iishi, P. H. Wu, T. Hatano, R. G. Mints, E. Goldobin, D. Koelle, H. B. Wang, and R. Kleiner, Phys. Rev. B **82**, 214506 (2010).
[27]R. A. Klemm, A. E. Davis, Q. X. Wang, T. Yamamoto, D. P. Cerkoney, C. Reid, M. L. Koopman, H. Minami, T. Kashiwagi, J. R. Rain, C. M. Doty, M. A. Sedlack, M. A. Morales, C. Watanabe, M. Tsujimoto, K. Delfanazari, and K. Kadowaki, IOP Conf. Ser.: Mater. Sci. Eng. **279**, 012017 (2017).
[28]R. A. Klemm and K. Kadowaki, J. Phys. Condens. Matter **22**, 375701 (2010).
[29]K. Kadowaki, M. Tsujimoto, K. Yamaki, T. Yamamoto, T. Kashiwagi, H. Minami, M. Tachiki, and R. A. Klemm, J. Phys. Soc. Jpn. **79**, 023703 (2010).
[30]M. Tsujimoto, K. Yamaki, T. Yamamoto, H. Minami, and K. Kadowaki, Physica C **470**, S779 (2010).
[31]Y. Demirhan, H. Saglam, F. Turkoglu, H. Alaboz, L. Ozyuzer, N. Miyakawa, and K. Kadowaki, Vacuum **120**, 89 (2015).
[32]C. A. Balanis, *Antenna Theory: Analysis and Design*, 3rd ed. (John Wiley & Sons, 2005).
[33]M. Haneishi, T. Nambara, and S. Yoshida, Electron. Lett. **18**, 191 (1982).
[34]H. Eisele, M. Naftaly, and J. R. Fletcher, Meas. Sci. Technol. **18**, 2623 (2007).
[35]M. Tsujimoto, I. Kakeya, T. Kashiwagi, H. Minami, and K. Kadowaki, Opt. Exp. 24, 4591 (2016).
[36]S. Gao, Q. Luo, and F. Zhu, *Circularly Polarized Antennas* (John Wiley & Sons, Ltd., Chichester, UK, 2014).

Superconductor Science and Technology

PAPER

Carrier doping into a superconducting $BaPb_{0.7}Bi_{0.3}O_{3-\delta}$ epitaxial film using an electric double-layer transistor structure

To cite this article: S Komori and I Kakeya 2018 *Supercond. Sci. Technol.* **31** 065004

IOP Publishing Superconductor Science and Technology

Supercond. Sci. Technol. **31** (2018) 065004 (5pp) https://doi.org/10.1088/1361-6668/aabb4c

Carrier doping into a superconducting $BaPb_{0.7}Bi_{0.3}O_{3-\delta}$ epitaxial film using an electric double-layer transistor structure

S Komori[1] and I Kakeya

Department of Electronic Science and Engineering, Kyoto University, Katsura, Nishikyo-ku, Kyoto 615-8510, Japan

E-mail: komori@sk.kuee.kyoto-u.ac.jp

Received 28 January 2018, revised 24 March 2018
Accepted for publication 3 April 2018
Published 27 April 2018

Abstract

Doping evolution of the unconventional superconducting properties in $BaBiO_3$-based compounds has yet to be clarified in detail due to the significant change of the oxygen concentration accompanied by the chemical substitution. We suggest that the carrier concentration of an unconventional superconductor, $BaPb_{0.7}Bi_{0.3}O_{3-\delta}$, is controllable without inducing chemical or structural changes using an electric double-layer transistor structure. The critical temperature is found to decrease systematically with increasing carrier concentration.

Keywords: EDLT, high temperature superconductivity, $BaBiO_3$

(Some figures may appear in colour only in the online journal)

1. Introduction

Several $BaBiO_3$-based compounds show three-dimensional high temperature superconductivity, whose critical temperature T_c, is much higher than that expected from their low carrier density. $Ba_{1-x}K_xBiO_{3-\delta}$ (BKBO) and $BaPb_{1-x}Bi_xO_{3-\delta}$ (BPBO) are two such compounds that show T_c's of 30 K [1] and 13 K [2], respectively, with carrier concentrations as low as 2×10^{21} cm^{-3} [3, 4]. The origin of their superconductivity is still open to much debate. Besides their low carrier concentration, $BaBiO_3$-based superconductors and cuprate superconductors share several similarities such as the existences of metal–insulator transition [5, 6], pseudogap phase [7, 8], and charge density wave (CDW) [8–10]. The relationship between these phenomena and the high temperature superconductivity they exhibit has been the subject of intensive study for several decades. The key to revealing these relationships is to understand the complex doping evolution of electric structures. In BKBO and BPBO, doping evolutions have been mainly studied by changing their chemical composition, x [1–6]. Although a decrease in K^+ and Pb^{4+} ions in BKBO and BPBO apparently seems to increase the number of electron carriers which will form Cooper pairs in the superconducting state, an increase in δ caused by charge compensation generates the CDW order and localizes electrons to the Bi site [11, 12]. This has been reported both in single crystals [13] and thin films [14]. The typical δ value of $BaBiO_{3-\delta}$ without K^+ and Pb^{4+} is around 0.5 [15] and it is known as a CDW insulator. Since a change in the chemical composition results in a corresponding change in both the carrier concentration and δ, the direct relationship among the carrier concentration, the CDW order and the superconducting properties has not been clarified in detail in $BaBiO_3$-based compounds.

In BPBO, the electron carrier concentration increases with increasing x and T_c becomes a maximum at $x = 0.3$ [2]. Increasing x beyond 0.3 leads to an increase in δ (and the CDW order), and a decrease in T_c. It has been reported that single-crystal BPBO is structurally dimorphic in the superconducting region ($x = 0.15$–0.35) and composed of phases with orthorhombic and tetragonal structures [16]. The tetragonal phase is believed to be responsible for the superconductivity because its volume fraction becomes maximum at optimally-doped region ($x = 0.3$) [16, 17]. However, the origin of the T_c-peak at $x = 0.3$ and how the carrier concentration affects T_c have not been fully understood yet.

[1] Author to whom any correspondence should be addressed.

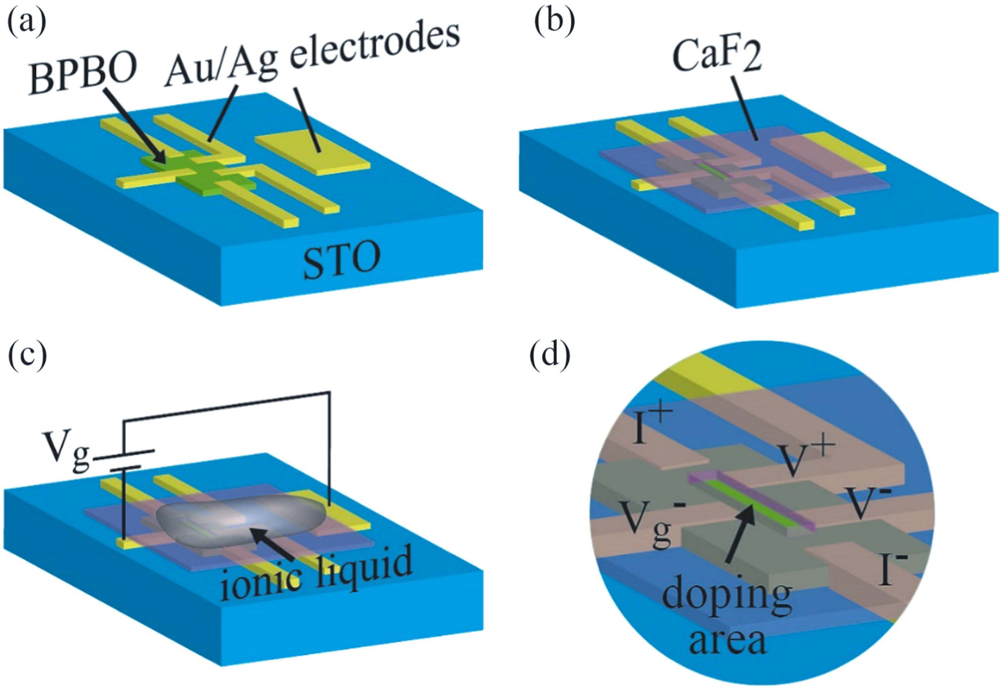

Figure 1. Schematic illustration of the device used in this work. (a) Patterned BPBO epitaxial film with Au/Ag electrodes. (b) The device after CaF_2 deposition. (c) The final structure of the device. The ionic liquid was placed over both the gate electrode and BPBO. (d) Enlarged illustration of the device structure around BPBO. On BPBO, there is an area which is not covered by CaF_2 to form the contact between BPBO and the ionic liquid.

In this work, we have carried out the electron doping for an optimally-doped superconducting BPBO epitaxial film with $x = 0.3$ using electric double-layer transistor (EDLT) structure [18–20] and investigated the relation between the T_c and the carrier concentration without changing the chemical composition. The maximum carrier concentration achieved by the doping is 3×10^{22} cm^{-3}, which is higher by an order of magnitude than that without the doping.

2. Experimental

A $BaPb_{0.7}Bi_{0.3}O_{3-\delta}$ (BPBO) epitaxial film was grown on an $SrTiO_3$ (100) substrate with an RF-magnetron sputtering system, which is generally used to grow $BaBiO_3$-based superconductors [4, 14, 21]. The substrate temperature was 650 °C and the atmosphere was 100 mTorr of the mixed gas of Ar:50% and O_2:50%. The cathode voltage was 1.4 kV. The approximate deposition rate was 30 nm min^{-1} and the total thickness of the film was 610 nm. After the deposition, the film was patterned into the size of $500 \times 100\ \mu m^2$ by laser lithography and an Ar ion milling technique. Subsequently, Au (50 nm)/Ag (15 nm) electrodes were fabricated by electron beam deposition and the lift-off technique, as shown in figure 1(a). Since the contact resistance of Ag/BPBO is much lower than that of Au/BPBO, Ag was deposited on BPBO first. To avoid an electro-chemical reaction of Ag and the ionic liquid, Au was subsequently deposited on Ag/BPBO. The electrodes around BPBO were covered by an insulating CaF_2 (200 nm) film to apply the electric field only on BPBO as represented in figure 1(b). The ionic liquid used in this work is DEME-TFSI (Kanto Chemical). At room temperature, the ionic liquid was placed over the BPBO and the gate electrode as illustrated in figure 1(c). The gate voltage, V_g, was applied in the range of ± 2 V to avoid inducing oxygen deficiencies due to the electro-chemical reactions. The carrier concentration and T_c controlled in this range were reversible. The transport properties of the device were measured by the physical properties measurement system. We found that the evacuation of air before cooling causes a dispersion of the ionic liquid, so low temperature measurements were performed under the ambient pressure of helium gas. The Hall carrier density was determined by a linear fit to the transverse resistivity as a function of the out-of-plane external magnetic field in the range of ± 5 T.

3. Results and discussion

To confirm the ideal crystallinity and the roughness of a BPBO epitaxial film, we collected and analyzed its x-ray diffraction patterns and atomic force microscope images. High resolution x-ray diffraction patterns confirmed the single orientation of BPBO with rocking curves on the (001), (002) and (003) Bragg peaks showing full width at half maximum values of 0.72°, 0.73°, and 0.56°, respectively; see figure 2(a). The c-axis lattice constant was determined to be 4.28 Å, which is consistent with the value obtained from the high resolution diffraction experiment for polycrystalline BPBO with $x = 0.3$ [22]. Figure 2(b) shows a typical atomic force microscope image of the BPBO film indicating an atomically

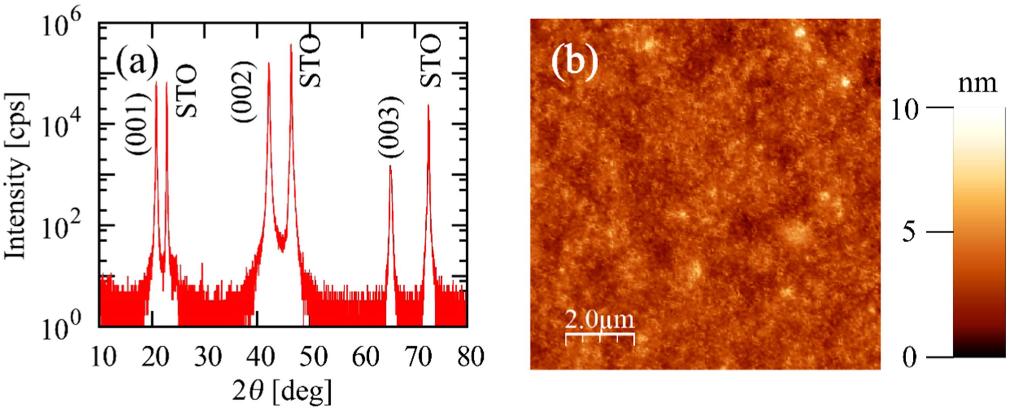

Figure 2. (a) θ–2θ x-ray diffraction pattern of BPBO on STO (001). (b) Atomic force microscope image of a BPBO epitaxial film.

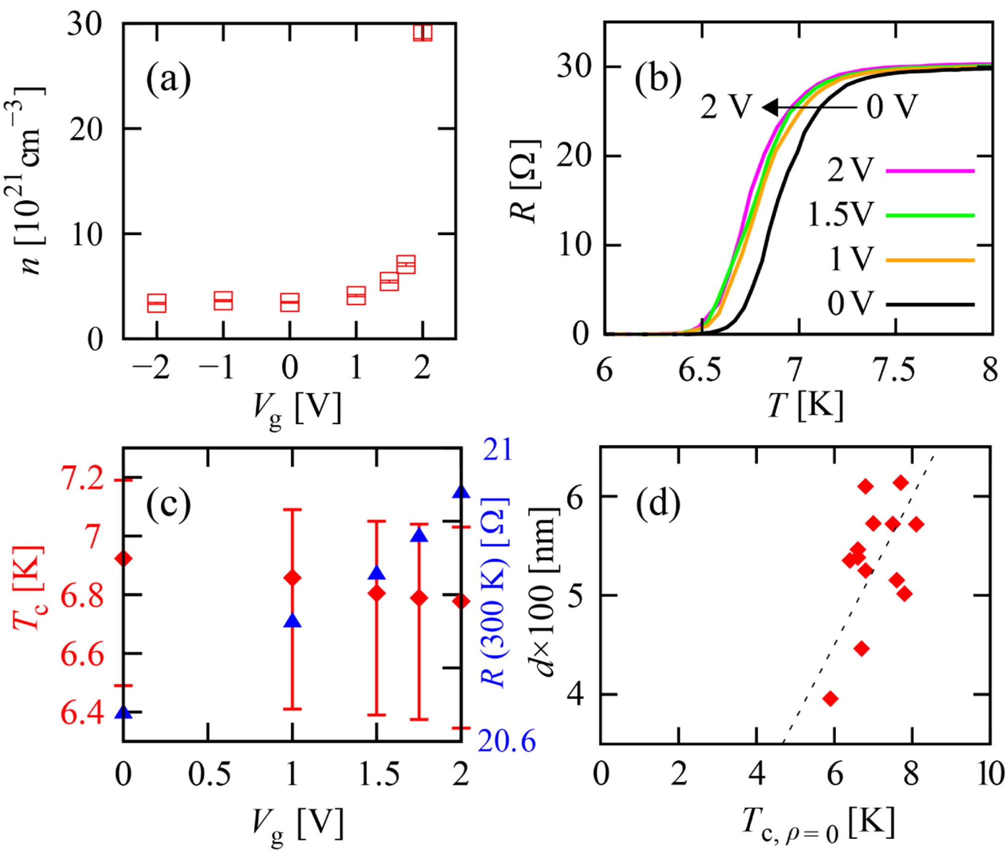

Figure 3. Gate voltage dependence of (a) Hall carrier concentration at 300 K, (b) resistance, (c) critical temperature (left axis, red diamonds), and room temperature resistance (right axis, blue triangles). The critical temperatures were extracted from 50% of the resistive transition. The vertical error bars for the critical temperatures show the width of the transition (from $T_{c,onset}$ to zero resistivity critical temperature, $T_{c,\rho=0}$). (d) Relation between the thickness and the critical temperature of BPBO epitaxial films. The dashed line is a guide to the eye.

flat surface with a root mean square roughness of about 1 nm over an area of 100 μm^2.

The Hall carrier density n, at 300 K with different V_g for the BPBO film is shown in figure 3(a). Although one might point out that Hall coefficient is not a direct measure of n for dimorphic BPBO, we assumed its homogeneous transport properties. The increase of n with increasing V_g indicates the carrier doping effect through EDLT. As shown in figure 4(a), anions in the ionic liquid accumulate around the positively biased gate electrode whereas cations accumulate around the negatively biased BPBO, which in turn results in the accumulation of electrons at the surface of BPBO. The change of the V_g from 0 to +2 V changes the carrier density of BPBO by an order of magnitude. Although positive V_g significantly affects n, negative V_g does not; this is because the carrier doping is not effective for the entire film, but only for the part of the film around the surface. The increase in the carrier density of the BPBO in the carrier doping region is observable through the decrease of its Hall resistivity. However, the decrease in the carrier density cannot be observed because

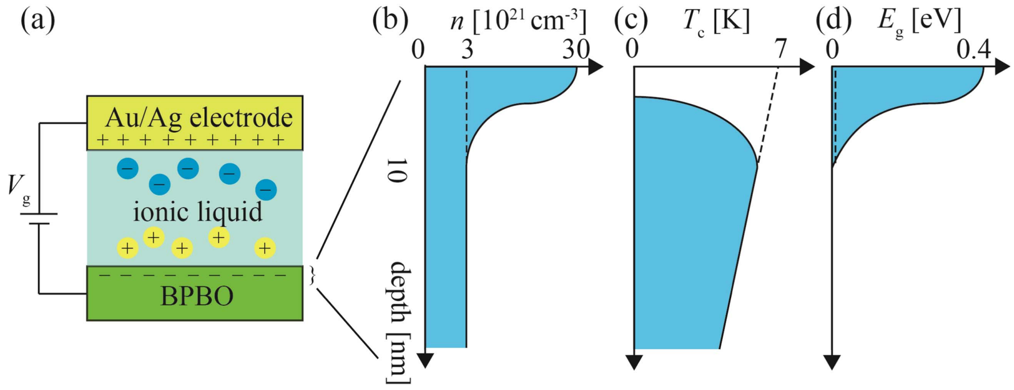

Figure 4. (a) Schematic diagram of the EDLT structure on BPBO. Depth profiles of (b) critical temperature, (c) electron concentration, and (d) CDW energy gap at around the surface of BPBO at $V_g = 2$ V. The dashed lines show the profiles for $V_g = 0$.

of the lower Hall resistivity in the rest part of the BPBO film that has a higher carrier concentration.

The temperature dependence of the resistivity around T_c with various V_g is shown in figure 3(b). It was found that T_c decreases and resistance increases with increasing V_g (carrier concentration), as plotted in figure 3(c). Here, T_c was defined by 50% of the resistive transition. A change of V_g from 0 to +2 V results in a decrease in T_c by 150 mK and an increase in the room temperature resistance by 1.5%. These changes were reversible, which rules out affects from any deteriorations of the film such as induction of oxygen deficiencies. Decrease in T_c is not easily observable in a superconductor which is thicker than the carrier doping layer because the T_c-suppression does not occur in the remaining part of the film under the carrier doping layer. However, in our device, the T_c-suppression is observable due to a large T_c-gradient in the film, even when the film is much thicker than the carrier doping layer. Since BPBO has a long coherence length ($\xi(0) = 7$ nm [4]) compared with cuprate superconductors ($\xi_c(0) = 0.3$–0.4 nm for $YBa_2Cu_3O_7$ [23] and $\xi_c(0) \sim 0.1$ nm for Bi-based cuprates[24]), its superconductivity is sensitive to impurities and strain in epitaxial films. Therefore, even in the 610 nm-thick film which was used in this work, T_c is much lower than that of single crystals. T_c of BPBO epitaxial films gradually increases with increasing thickness as shown in figure 3(d). This is considered to be due to a gradual decrease in the density of crystal defects caused by the strain in epitaxial films. The low-T_c region near the BPBO/STO interface can be proximitized by high-T_c region near the surface which has relatively high carrier concentration. This can also result in a T_c-gradient in epitaxial films.

The 1.5% increase in the resistance by the application of $V_g = +2$ V can be translated to an appearance of the highly resistive carrier doping layer with the thickness of 9 nm (1.5% of the total 610 nm). The 1.5% resistance shift was observed down to the onset temperature of the superconducting transition $T_{c,onset}$, suggesting that the thickness of the carrier doping layer does not depend strongly on the temperature. This can be due to the small change (10%) of the Hall carrier concentration between room temperature and $T_{c,onset}$ in BPBO ($x = 0.3$) epitaxial films [4]. The linear suppression of T_c with increasing V_g despite the nonlinear increase in the carrier concentration implies the nonlinear relation between the carrier concentration and the thickness of the doping layer. The thickness of the carrier doping layer is determined by the charge screening length, which depends on the carrier concentration, dielectric constant, and effective mass of materials. A typical charge screening length for semiconductors is few nanometers, which corresponds to the length scale of the band bending effect at the surface of semiconductors. The carrier doping layer of 9 nm estimated for BPBO in this work is longer than the typical charge screening length. However, it is worth noting that in some doped Mott insulators such as VO_2 [25], $NdNiO_3$ [26], and $Pr_{1-x}Sr_xMnO_3$ [27], the charge screening length of several tens of nanometers has been reported. This is considered to be due to the metal–insulator transition at the interface induced by the carrier doping. Since the electric states of a metallic phase and an insulating phase are significantly different, energy band structures of the bulk and surface becomes discontinuous by the carrier doping. The energy band structure of the surface is gradually relaxed to that of the bulk and this relaxation length is considered to be longer than the charge screening length. This can enable the long-range control of the electronic state by EDLT in Mott insulators including BPBO.

Finally, we discuss the details of the carrier doping effect in the BPBO epitaxial film. The carrier concentration of BPBO at $x = 0$ is as low as 3×10^{20} cm^{-3} due to a small amount of the density of states at the Fermi level in Pb(6s)-O (2p) hybrid bands. Substitution of $Bi^{4+}(6s)^1$ for $Pb^{4+}(6s)^0$ (i.e., increasing x) results in electron doping and an increase in T_c until $x = 0.3$ [4]. However, the resistivity increases with increasing x [4, 28]. This is explained by the formation of CDW order in which BiO_6 octahedra exhibit breathing distortions. The energy gap of the CDW insulating order increases with increasing x (δ) and results in the suppression of T_c at $x > 0.3$. Eventually, the superconductivity disappears at around x = 0.35 ($\delta = 0.18$) [4, 28]. In this work, electron doping for the sample with $x = 0.3$ was found to decrease T_c as illustrated in figures 4(b) and (c). In addition, a decrease in the resistivity was not observed in spite of the significant increase in the carrier concentration. In high temperature cuprate superconductors, an increase in n by an order of magnitude drastically decreases their resistivity. In $La_{2-x}Sr_xCuO_4$, an increase in n from 3×10^{21} to 3×10^{22} cm^{-3} observed in this work corresponds to a change from $x = 0.13$ (slightly underdoped) to $x = 0.25$ (highly overdoped) [29], which reduces the resistivity by a factor of 3 [30]. Here, the Sr concentration x corresponds to the effective number of holes per Cu atom in the CuO_2 superconducting layer. However, in this work, the resistivity of the BPBO film was not decreased but increased by 1.5%, suggesting that the surface of the BPBO film became more resistive due to the electron doping. This trend is similar to the Bi substitution effect that increases both the carrier concentration and the resistivity. The most plausible interpretation of the results in this work is that the electron doping into Bi^{5+} ions has increased the concentration of Bi^{3+} ions and led to an enhancement of the CDW order which is generated by an alternating array of Bi^{3+} and Bi^{5+} ions. In BPBO, it has been reported that the CDW energy gap E_g [eV] roughly follows $E_g = 0.7x - 0.3$ [31]. Application of $V_g = 1.75$ V increased the carrier concentration of the device to 8×10^{21} cm^{-3}, which is the value for $BaBiO_3$ ($x = 1$). This allows for the generation of a CDW gap of 0.4 eV (the value for $x = 1$) as illustrated in figure 4(d) and leads to an increase in the normal state resistivity. Considering the fact that the Bi substitution for $x = 0.3$ film increases E_g and suppresses T_c, it is highly possible that the T_c-suppression observed in this work is due to the formation of the CDW order.

4. Conclusions

We have observed the carrier doping effect in a $BaBiO_3$-based unconventional superconductor by using an EDLT structure for the first time. An increase in the electron doping level from 3×10^{21} to 3×10^{22} cm^{-3} was observed in a $BaPb_{0.7}Bi_{0.3}O_{3-\delta}$ epitaxial film. It was found that the increase in the carrier concentration results in the suppression of the superconductivity and the increase in the normal state resistivity. T_c-decrease of 150 mK and 1.5%-increase in the room temperature resistivity were observed in the 610 nm-thick film.

Acknowledgments

The authors deeply thank Y Matsumoto, Y Kamei, A Uzawa, Y Nakagawa and M Suzuki for experimental support and fruitful discussions. This work was financially supported by the JSPS KAKENHI Grant No.15J07623.

ORCID iDs

S Komori https://orcid.org/0000-0002-8288-6786

References

[1] Cava R J, Batlogg B, Krajewski J J, Farrow R, Rupp L W J, White A E, Short K, Peck W F and Kometani T 1988 *Nature* **332** 814–6
[2] Sleight A W, Gillson J L and Bierstedt P E 1975 *Solid State Commun.* **17** 27–8
[3] Hellman E S and Hartford E H Jr 1993 *Phys. Rev.* B **47** 11346–53
[4] Suzuki M 1993 *Japan. J. Appl. Phys.* **32** 2640–7
[5] Khosroabadi H, Miyasaka S, Kobayashi J, Tanaka K, Uchiyama H, Baron A Q R and Tajima S 2011 *Phys. Rev.* B **83** 224525
[6] Namatame H, Fujimori A, Takagi H, Uchida S, de Groot F M F and Fuggle J C 1993 *Phys. Rev.* B **48** 16917–25
[7] Namatame H, Fujimori A, Torii H, Uchida T, Nagata Y and Akimitsu J 1994 *Phys. Rev.* B **50** 13674–8
[8] Tajima S, Uchida S, Masaki A, Takagi H, Kitazawa K and Tanaka S 1987 *Phys. Rev.* B **35** 696–703
[9] Le T M, Bosak A, Souliou S M, Dellea G, Loew T, Heid R, Bohnen K, Ghiringhelli G, Krisch M and Keimer B 2014 *Nat. Phys.* **10** 52–8
[10] Du C-H and Hatton P D 1995 *Europhys. Lett.* **31** 145–50
[11] Balzarotti A, Menushenkov A, Motta N and Purans J 1984 *Solid State Commun.* **49** 887–90
[12] Anderson P W 1975 *Phys. Rev. Lett.* **34** 953–5
[13] Idemoto Y, Iwata Y and Fueki K 1992 *Physica* C **201** 43–9
[14] Suzuki M and Murakami T 1985 *Solid State Commun.* **53** 691–4
[15] Hashimoto T, Kobayashi T, Tanaka H, Hirasawa R, Hirai H and Tagawa H 1998 *Solid State Ion.* **108** 371–6
[16] Climent-Pascual E, Ni N, Jia S, Huang Q and Cava R J 2011 *Phys. Rev.* B **83** 174512
[17] Marx D T, Radaelli P G, Jorgensen J D, Hitterman R L, Hinks D G, Pei S and Dabrowski B 1992 *Phys. Rev.* B **46** 1144–57
[18] Ueno K, Nakamura S, Shimotani H, Ohtomo A, Kimura N, Nojima T, Aoki H, Iwasa Y and Kawasaki M 2008 *Nat. Mater.* **7** 855–8
[19] Shimotani H, Asanuma H, Tsukazaki A, Ohtomo A, Kawasaki M, Shimotani H, Asanuma H, Tsukazaki A and Ohtomo A 2010 *Appl. Phys. Lett.* **91** 82106
[20] Bollinger A T, Dubuis G, Yoon J, Pavuna D, Misewich J and Bozovic I 2011 *Nature* **472** 458–60
[21] Iyori M, Suzuki S, Suzuki H, Yamano K, Takahashi K, Usuki T, Yoshisato Y and Nakano S 1993 *Japan. J. Appl. Phys.* **32** 1946–51
[22] Sleight A W 2015 *Physica* C **514** 152–65
[23] Welp U, Kwok W, Crabtree G, Vandervoort K and Liu J 1989 *Phys. Rev. Lett.* **62** 1908–11
[24] Matsushita T 1993 *Physica* C **205** 289–95
[25] Nakano M, Shibuya K, Okuyama D, Hatano T, Ono S, Kawasaki M, Iwasa Y and Tokura Y 2012 *Nature* **487** 459–62
[26] Asanuma S *et al* 2015 *Appl. Phys. Lett.* **97** 142110
[27] Hatano T, Ogimoto Y, Ogawa N, Nakano M, Ono S, Tomioka Y, Miyano K, Iwasa Y and Tokura Y 2013 *Sci. Rep.* **3** 2904
[28] Uchida S, Kitazawa K and Tanaka S 1987 *Phase Transit.* **8** 95–128
[29] Padilla W J, Lee Y S, Dumm M and Blumberg G 2005 *Phys. Rev.* B **72** 60511
[30] Boebinger G, Ando Y, Passner A, Kimura T, Okuya M, Shimoyama J, Kishio K, Tamasaku K, Ichikawa N and Uchida S 1996 *Phys. Rev. Lett.* **77** 5417–20
[31] Uwe H, Minami H, Nishio T, Ahmad J and Shizuya M 2007 *Ferroelectrics* **346** 1–9

27P2-2

銅酸化物高温超伝導体における集団的固有ジョセフソン現象

Evolution of collective inter-layer intrinsic Josephson phenomena in cuprate superconductors

Itsuhiro Kakeya

Department of Electronic Science and Engineering, Kyoto University

In curate superconductors, rich varieties of quantum phenomena are observed in the *c*-axis transport properties because their crystal structures are alternations of a unit of CuO_2 planes, where the superconducting order parameter is localized, and a unit of insulating metal-oxide planes participating as a charge reservoir for their superconductivity. This alternation of superconducting and insulating layers, a stack of intrinsic Josephson junction (IJJ) [1], has been providing surprising phenomena such as macroscopic quantum tunneling up to 1 K [2] and emissions of terahertz electromagnetic waves with powers up to 0.6 mW [3], which are potentially applied for quantum devices. However, most of results reported so far are obtained in $Bi_2Sr_2CaCu_2O_8$ (Bi2212) with double CuO_2 planes for a superconducting layer, thus phenomena in other superconductors have been interpreted to be scaled by their superconducting anisotropies.

We have investigated IJJ properties measured along the *c*-axis of three materials with different numbers of CuO_2 planes in a superconducting layer (n = 1, 2, 3). In Bi2201 and Bi2212, we found a collective phenomenon between adjacent IJJs, which is explained by introducing a short range interaction between IJJs due to the breaking of charge neutralization of superconducting layers (capacitive coupling) [4]. In Bi2223, no explicit phenomenon attributed to the capacitive coupling has found. However, we found the scalable description of IJJ is no longer valid and the distribution of superconducting electron density allows to describe IJJ properties of Bi2223 totally [5].

[1] R. Kleiner, F. Steinmeyer, G. Kunkel and, P. Müller Phys. Rev. Lett. **68** 2394 (1992).

[2] K. Inomata et al., Phys. Rev. Lett. **95** 107005 (2005).

[3] L. Ozyuzer, et al., Science **318** 1291 (2007); I. Kakeya and H.-B. Wang, Supercond. Sci. Technol. **29** 073001 (2016).

[4] Y. Nomura et al., J. Phys. Soc. Jpn. **84** 013704 (2015); Y. Nomura et al., Supercond. Sci. Technol. **30** 105001 (2017).

[5] Y. Nomura et al., J. Phys.: Conf. Ser. **507**, 012038 (2014); Y. Nomura et al., in preparation.